Electronic Supplementary Material (ESI) for CrystEngComm.

Supporting Information

Exploration of MOF nanoparticles sizes using various physical characterisation methods - Is what you measure what you get?

Patrick Hirschle,[a] Tobias Preiß,[b] Florian Auras,[a] André Pick,[c] Johannes Völkner,[c] Daniel Valdepérez,[c] Gregor Witte,[c] Wolfgang J. Parak,[c] Joachim O. Rädler,[b] and Stefan Wuttke[a]*

[a] *Department of Chemistry and Center for NanoScience (CeNS), University of Munich (LMU), Butenandtstraße 11, 81377 Munich*

[b] *Department of Physics and Center for NanoScience (CeNS), University of Munich (LMU), Geschwister-Scholl-Platz 1, 80539 Munich*

[c] *Faculty of Physics, Philipps University Marburg, Renthof 7, 35037 Marburg*

Correspondence to:

stefan.wuttke@cup.uni-muenchen.de

Table of Contents

1 Methods and Characterisation

Thermogravimetry (TG): A dried sample of Zr-*fum* (6.3 mg) was examined on a *TASC 414/4* (*Netzsch*). The thermogravimetric experiment was performed with a heating rate of 10 °C/min up to 900 °C. The results were evaluated using the included software Proteus v4.3.

Nitrogen Sorption: Dried powder of Zr-fum (6.3 mg) was degassed for 12 h at 120 °C in high vacuum. Subsequently, nitrogen sorption was performed on the sample using an Autosorb-1 (Quantachrome). The results were evaluated using the software ASiQwin v3.0. Brunauer-Emmett-Teller (BET) surface areas[1] were calculated by using the linearised form of the BET equation. A correlation coefficient of r = 0.999755 was achieved. The pore size distribution of the sample was determined by using the software`s non-local density functional theory (NLDFT) equilibrium model based on slit and cylindrical pores.

Scanning Electron Microscopy (SEM): The experiments, which are presented here, were performed on a *Jeol JSM-6500F* with EDX-Detektor and *Inca*-software (*Oxford Instruments*). For sample preparation, an ethanolic dispersion of the Zr-*fum* nanoparticles was dried and subsequently sputtered with carbon. The resulting micrographs were evaluated manually using the software *ImageJ v1.49*.

Transmission Electron Microscopy (TEM): All of the experiments were performed on a *Tecnai G2* (*Fei*) with an acceleration voltage of 200 kV. For sample preparation, a dispersion of the Zr-*fum* nanoparticles in ethanol was dried on a carbon-coated copper grid. The resulting micrographs were evaluated manually by using the software *ImageJ v1.49*. The micrographs shown in Figure S5 and Figure S9-Figure S13 have been measured in imaging mode. The electron diffraction patterns shown in Figure S6-Figure S8 have separately been recorded in separately diffraction mode.

Atomic Force Microscopy (AFM): Epi-ready silicon wafers coated with a native oxide (Siegert Wafer GmbH) were used as ultraflat supporting substrates. Initially, all supports were cleaned in an ultrasonic bath in ethanol and subsequently blown dry in a nitrogen stream. 2 µL of the nanoparticle solution were pipetted onto a substrate. Slow evaporation of the solvent at room

temperature led to a concentric density gradient of the nanoparticles deposited on the surface. The morphology of nanoparticles was characterised by means of atomic force microscopy using a SPM5500-AFM instrument (Agilent) operated in closed loop tapping mode at ambient conditions, and using HQ:NSC15/AlBS cantilevers (MikroMasch; resonance frequency, 325 kHz). The z-range of the scanner had been carefully calibrated using a standard silicon grating with a step height of 84.3 nm and an accuracy of 1.5 nm.

X-Ray Diffraction (XRD): Powder X-ray diffraction (PXRD) measurements were performed using a Bruker D8 Discover with Ni-filtered Cu K_α radiation and a LynxEye position-sensitive detector. In order to reduce the peak broadening caused by the instrument to a minimum, 0.05 mm and 3 mm slits were installed at the X-ray tube assembly and the detector, respectively. In conjunction with a detector opening of 0.8 °, the instrument broadening was thus reduced to 0.05 ° 2ϑ (calibrated against LaB_6). The Pawley fitting[2] of the resulting data treats peak areas as variables. Hence, they were not being used for atom-position refinement. Only the unit cell size *a* and the crystallite size *d* were refined. The reflections were assumed to feature a Pseudo-Voigt profile and peak asymmetry was corrected using the Berar-Baldinozzi function.

Dynamic Light Scattering (DLS): During the experiments, all DLS measurements were performed on a *Zetasizer Nano Series* (Nano-ZS, *Malvern*). The employed laser operated at a wavelength λ = 633 nm. The measurement of Zr-*fum* was conducted directly after washing the freshly synthesised nanoparticles. For the respective measurement, the sample dispersion in ethanol was diluted in ethanol (1:200) or water (1:200).

Fluorescence Correlation Spectroscopy: All experiments were conducted on an Axiovert 200M equipped with a ConfoCor2 unit (Carl Zeiss), using a 40x NA1.2 water immersion objective and an argon ion laser at 488 nm wavelength. Emitted light was separated from excitation light with a dichroic mirror and a bandpass emission filter (505 – 550 nm). Samples were prepared and measured in Nunc 8 well plates (Thermo Scientific). The focal width w = 0.2 µm was determined by a calibration measurement using Alexa Fluor 488 with a known diffusion coefficient of D = 435 µm²/s. [3] Samples of three individually produced batches of Zr-*fum* were investigated with FCS. For this purpose Zr-*fum* nanoparticles were fluorescently labeled by adding 20µL of

Zr-*fum* dispersed in ethanol suspension to 200 µL of an Alexa Fluor 488 solution. After 10 minutes of incubation FCS measurements were performed. To avoid singe particle aggregates, which would distort the correlation curves, the so called dust filter of the instrument's software (70%) was used. By this the fluorescence fluctuations are analysed prior to correlation and spikes caused by agglomerated particles having a deviation of more than 70% from the average count rate within a binned count rate time are cut out and not used for the correlation analysis similar to the method described by Persson *et al.* (2009).[4]

2 Experimental Section

2.1 Chemicals

The chemicals Zr(IV) chloride (≥ 95 %, Aldrich), formic acid (> 85 %, Aldrich), fumaric acid (≥ 99.5 %, Fluka) and ethanol (99.9 %, VWR) were all used without further purification.

2.2 Synthesis of Zr-*fum* samples

$ZrCl_4$ and Fumaric acid (see Table S1) were put into a glass reactor (25 mL). A mixture of water (10 mL) and formic acid (975 µL) was added to the educts. The reactor was then sealed and placed in an oven at 120 °C for 24 h.

After cooling down, the resulting white precipitate was washed. The dispersion was divided into 8 vials (1.5 mL), and then centrifuged (14000 rpm, 5 min). After discarding the supernatants, the precipitates were redispersed in water (1.25 mL per precipitate) via sonication. The dispersions were centrifuged (14000 rpm, 5 min) and the supernatants removed. The precipitates were redispersed in ethanol (1.25 mL per precipitate). After repeating this last washing cycle for an additional washing cycle the ethanol-based dispersions were unified.

Table S1 | Weight-ins of the respective Zr-*fum* batches.

Sample	m($ZrCl_4$) [mg]	m(fumaric acid) [mg]
Zrfum-1	120.9	180.4
Zrfum-2	120.4	180.2
Zrfum-3	120.6	180.4
Zrfum-4	120.5	180.3

2.3 Characterisation of Zr-*fum*

Structure of Zr-*fum*

As reported by Wißman *et al.*[5] the microporous, cubic structure of Zr-*fum* featuring the formula $Zr_6O_4(OH)_4(O_2C\text{-}(CH)_2\text{-}CO_2)_6$ displays the space group $Pn\bar{3}$. The X-ray diffraction experiments conducted in this work (see Figure S14) have resulted in a lattice parameter of a = (17.91 ± 0.03) nm to (17.88 ± 0.03) nm.

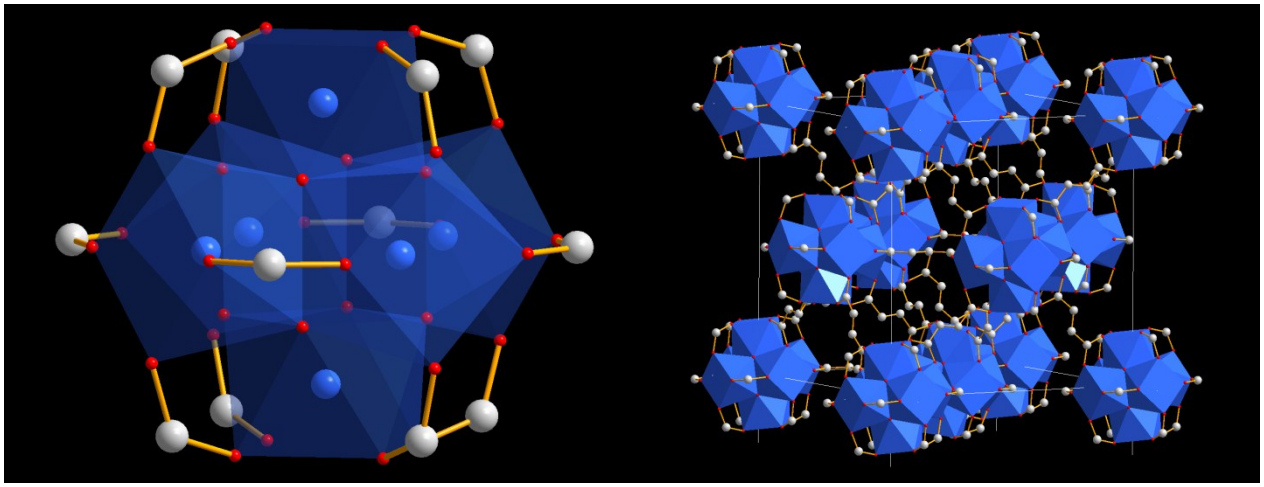

Figure S1 | Secondary building unit (left) and architecture (right) of Zr-*fum*; Zr (*blue*), O (*red*), C (*grey*).

Figure S1 shows the composition of the structure and the position of the secondary building units (SBUs) on the vertices and faces of a cubic cell. Each SBU comprises of 6 Zr-atoms (*blue*) that are octahedrally aligned and coordinated by 8 oxygen-atoms (*red*). The carbon atoms (*grey*) are the first segment of the emerging fumaric acid linker chains, which are arranged cuboctahedrally and thereby connecting each SBU to 12 neighboring clusters.

Nitrogen sorption

The Zr-*fum* nanoparticles displayed a specific BET surface area of 408 $m^2 \cdot g^{-1}$. The pore size distribution (see Figure S2) was determined to feature a maximum at the pore with d = 0.57 nm. The corresponding nitrogen sorption graph (see Figure S2) can be identified as an IUPAC Type I microporous adsorption isotherm.[6]

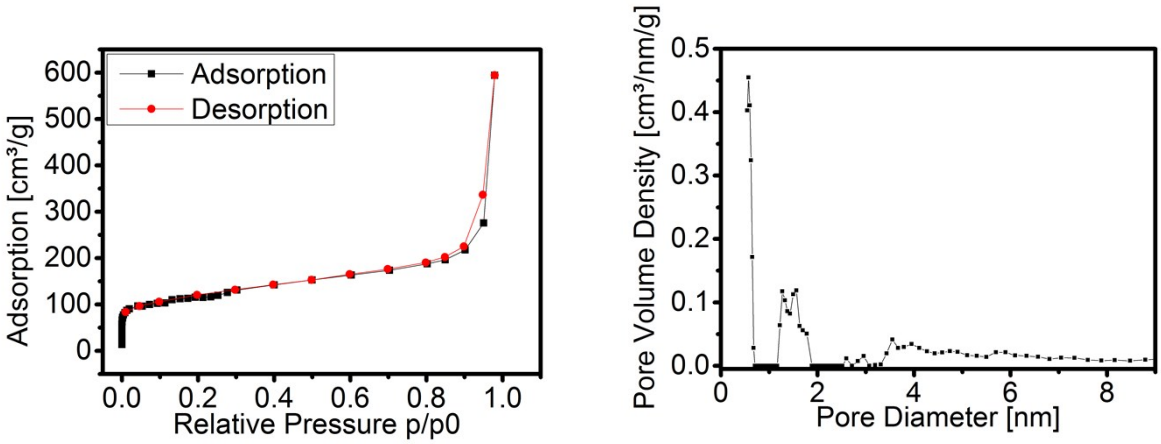

Figure S2 | Nitrogen sorption isotherm showing the adsorption of nitrogen in dependency of its relative pressure (left) and the differential pore size distribution in dependency of the pore-diameter (right).

Thermogravimetry

From 48 °C to 250 °C a mass loss occurred which was probably caused by desorption of water from the framework. At 260 °C the decomposition of the organic linker began, similar to the decomposition of pure fumaric acid at 200 °C as reported by Wißman *et al.*[5] This decomposition-step was finished at 480 °C. Subsequently at around 600 °C a final mass loss occurred, which was finished at around 750 °C. Comparing the TG measurement with the data published by Wißman *et al.*, similarities can be seen: they report a similar decomposition range for the linker starting at 250 °C and ending at 400 °C. Wißman *et al.* also provide an explanation for the final mass loss: CO_2 is released from the decomposition of carboxylate groups. Overall, this mass loss caused by the sample during the decomposition of the linker and release of CO_2 is at 47.5 %, which is in a good agreement with the calculated results at 45.8 %.[5] The corresponding graph is shown in Figure S3.

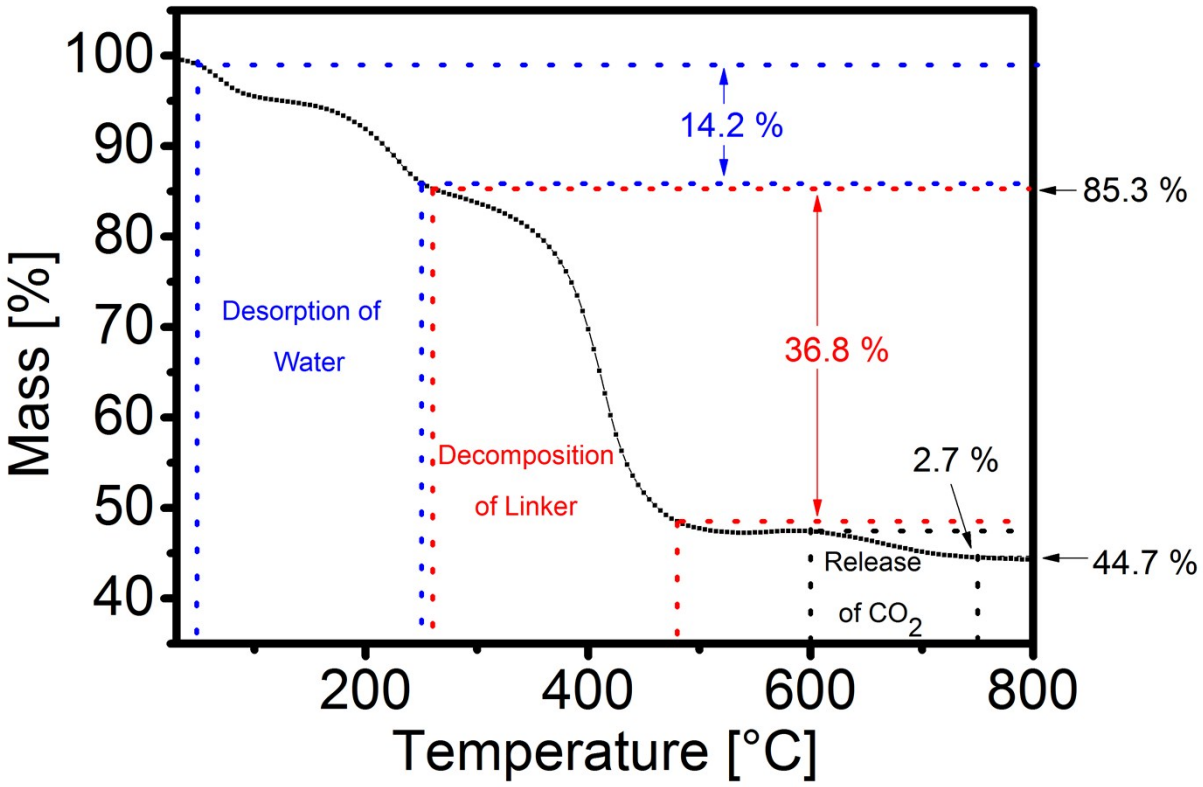

Figure S3 | Thermogravimetric evaluation of Zr-*fum*.

Scanning Electron Microscopy

The image, which is used to obtain the SEM size distribution, is shown in Figure S4.

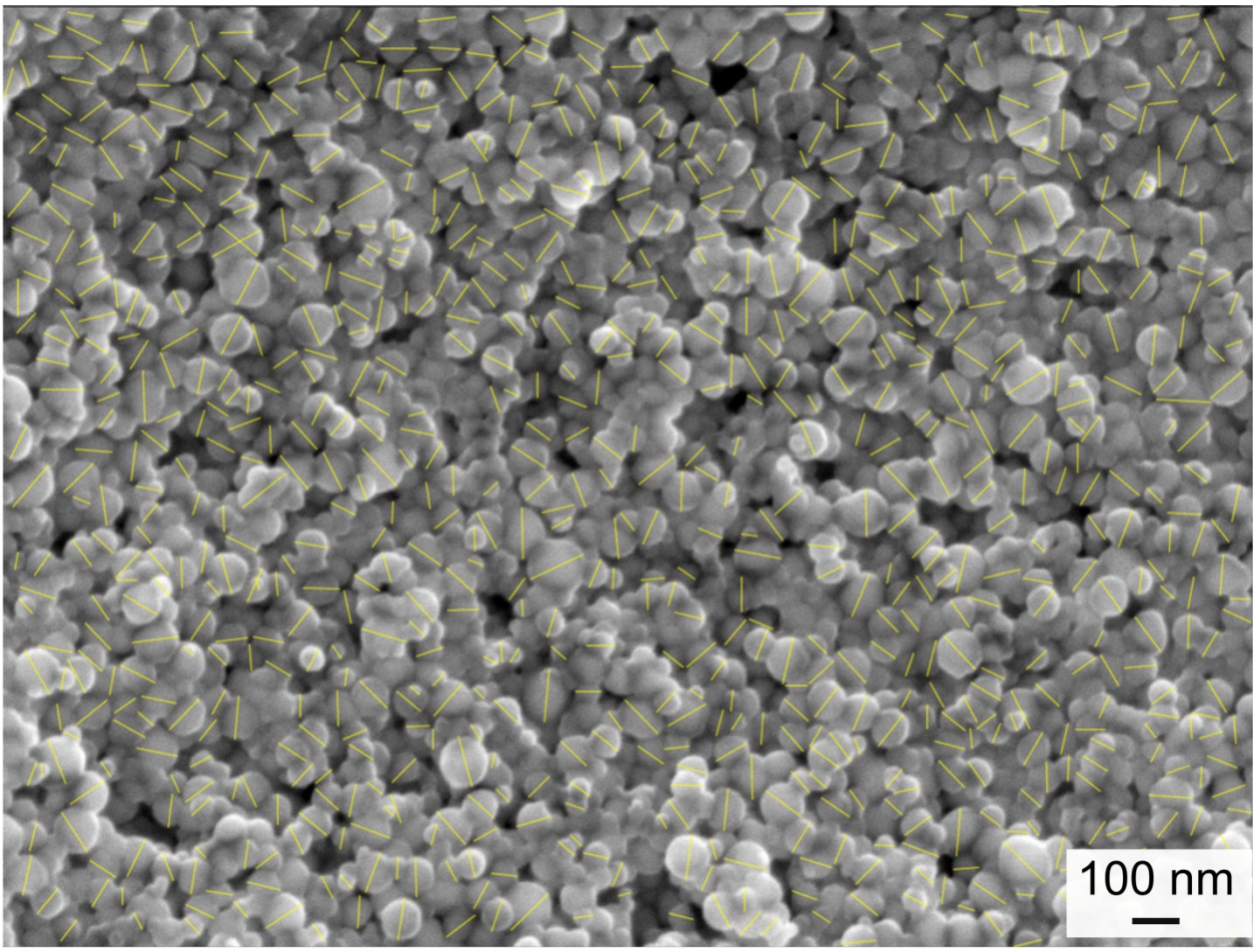

Figure S4 | Zr-*fum* particles measured for SEM size determination.

Transmission Electron Microscopy

An overview picture of dried Zr-*fum* nanoparticles is shown in Figure S5.

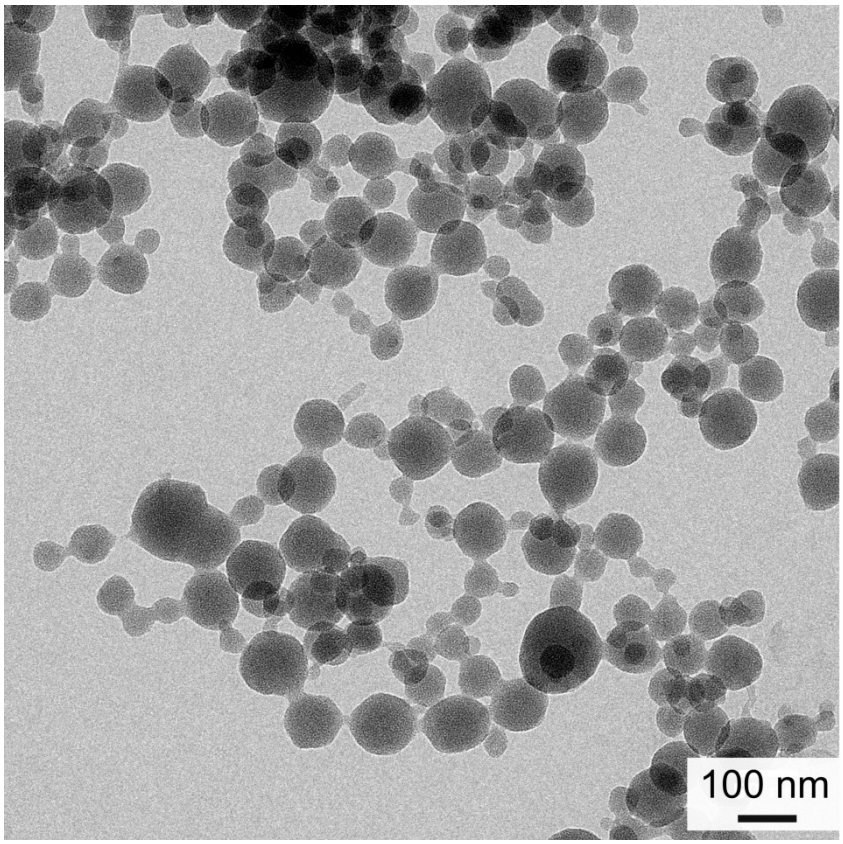

Figure S5 | Overview picture of Zr-*fum.*

Figure S6, Figure S7, and Figure S8 show Zr-fumarate when exposed to an electron beam (200 keV) for a prolonged period of time. The Debye-Scherrer rings, which are initially still recognisable after an exposure time of 6.5 s, gradually disappear indicating the damage the sample is taking from the electron beam.

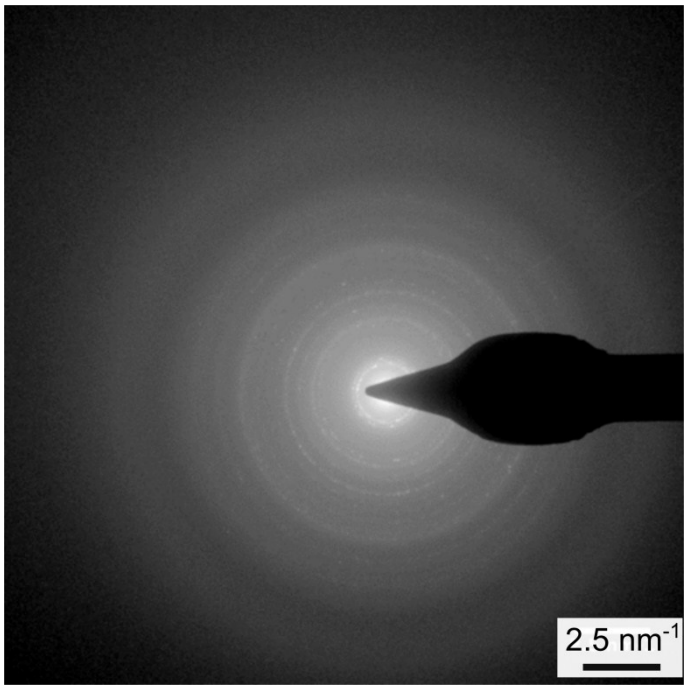

Figure S6 | Electron diffraction pattern of sample Zr-*fum* after 6.5 seconds in a 200 kV electron beam.

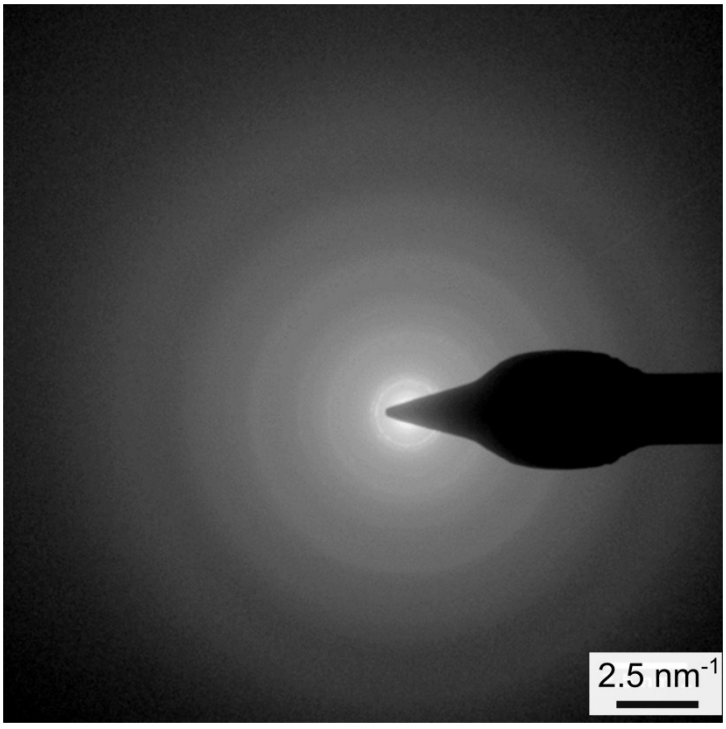

Figure S7 | Electron diffraction pattern of sample Zr-*fum* after 13 seconds in a 200 kV electron beam.

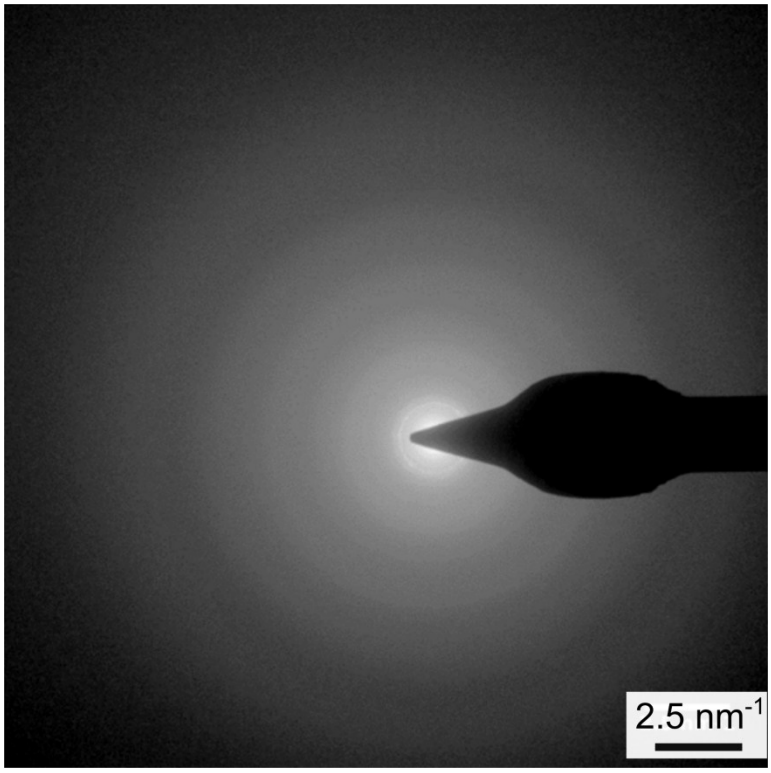

Figure S8 | Electron diffraction pattern of sample Zr-*fum* after 26 seconds in a 200 kV electron beam.

In Table S2 the Debye-Scherrer rings of Zr-*fum* shown in Figure S6 are shown along with their corresponding HKL indices and interplanar spacings *d*. They are in good agreement with the crystallographic data published by Wißmann *et al.*[5], which verifies the successful synthesis of Zr-fumarate MOF nanoparticles.

Table S2 | Diffraction rings of Zr-*fum* with their indices and interplanar spacing.

Diffraction Ring	***d (experiment)* [Å]**	**HKL**	**d (literature)[4] [Å]**	**deviation [%]**
1	10.1365	(111)	10.3591	2.1
2	8.7538	(200)	8.9545	2.2
3	4.3961	(400)	4.4776	1.8
4	4.0201	(331)	4.1084	2.1
5	3.5727	(422)	3.6554	2.3
6	3.3966	(333)	3.4466	1.5
7	2.9373	(600)	2.9847	1.6
8	2.6755	(533)	2.7312	2.0
9	2.5374	(444)	2.5850	1.8
10	2.4732	(551)	2.5081	1.4
11	2.2804	(553)	2.3315	2.2

The particles that were measured to determine the TEM size distribution are shown in Figure S9, Figure S10, Figure S11, Figure S12, and Figure S13.

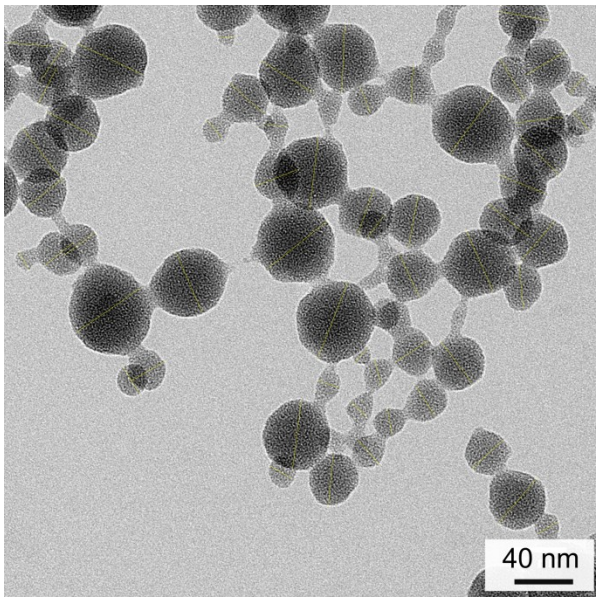

Figure S9 | Zr-*fum* particles measured for TEM size determination.

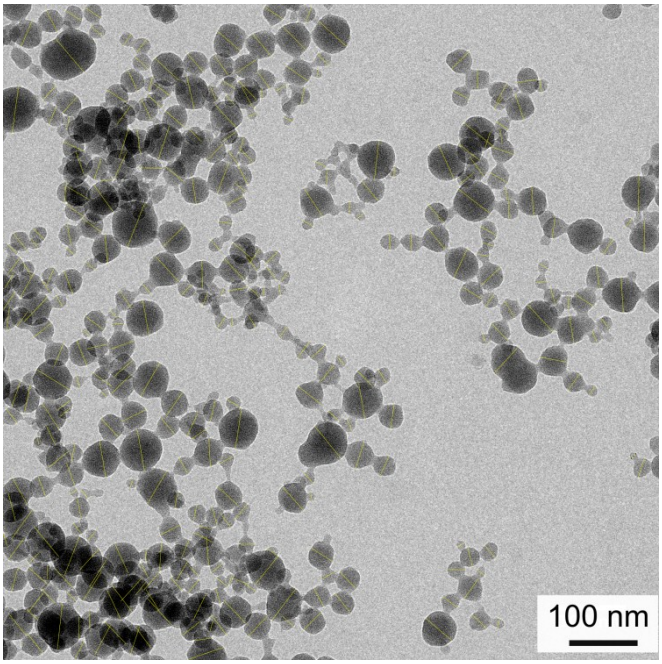

Figure S10 | Zr-*fum* particles measured for TEM size determination.

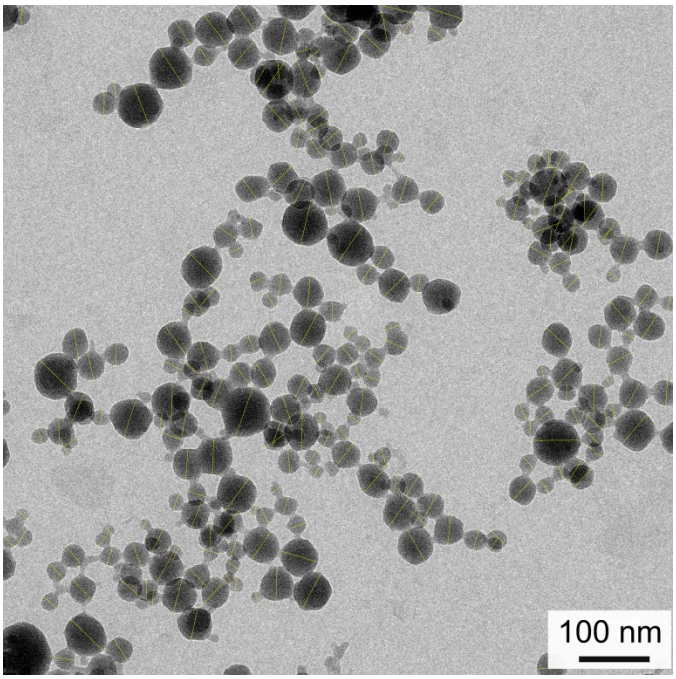

Figure S11 | Zr-*fum* particles measured for TEM size determination.

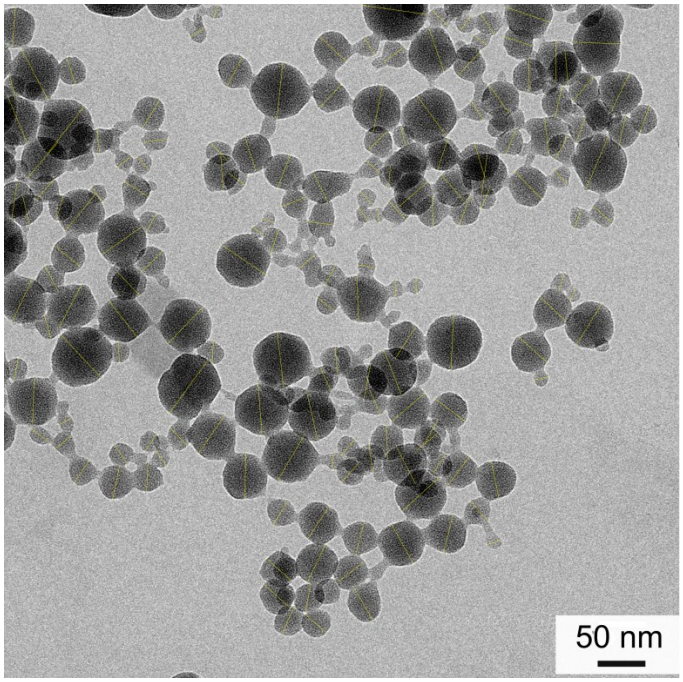

Figure S12 | Zr-*fum* particles measured for TEM size determination.

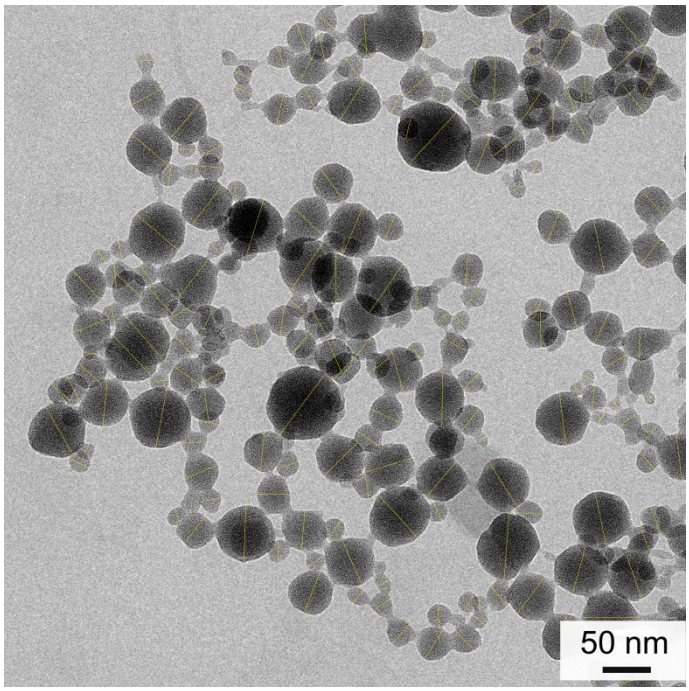

Figure S13 | Zr-*fum* particles measured for TEM size determination.

X-Ray Diffraction

The theoretical PXRD pattern of the Zr-*fum* MOF was simulated using the structure model and atomic coordinates reported by Wißmann *et al*.[5] and assuming a domain size of 50 nm.

The results of the X-ray diffraction experiments for samples Zrfum-1, Zrfum-2, Zrfum-3 and Zrfum-4 are shown in Figure S14. The corresponding average size of the crystalline domains is shown in Table S2. Besides slightly smaller crystalline domains for sample Zrfum-3, the crystalline domains of the sample generally feature a similar size, which confirms the good reproducibility of the aqueous synthesis.

Pawley fitting of the experimental PXRD data was carried out using in the Reflex module of the Accelrys Materials Studio software and refining the unit cell parameter *a* and the domain size *d*. We used Pseudo-Voigt peak shape functions with fixed profile parameters (determined from measurements of a LaB_6 micropowder sample). Peak asymmetry was corrected using the Berar-Baldinozzi function. Overlay of the observed and refined profiles shows very good correlation with small deviations at low angles, where the peak asymmetry is more pronounced.

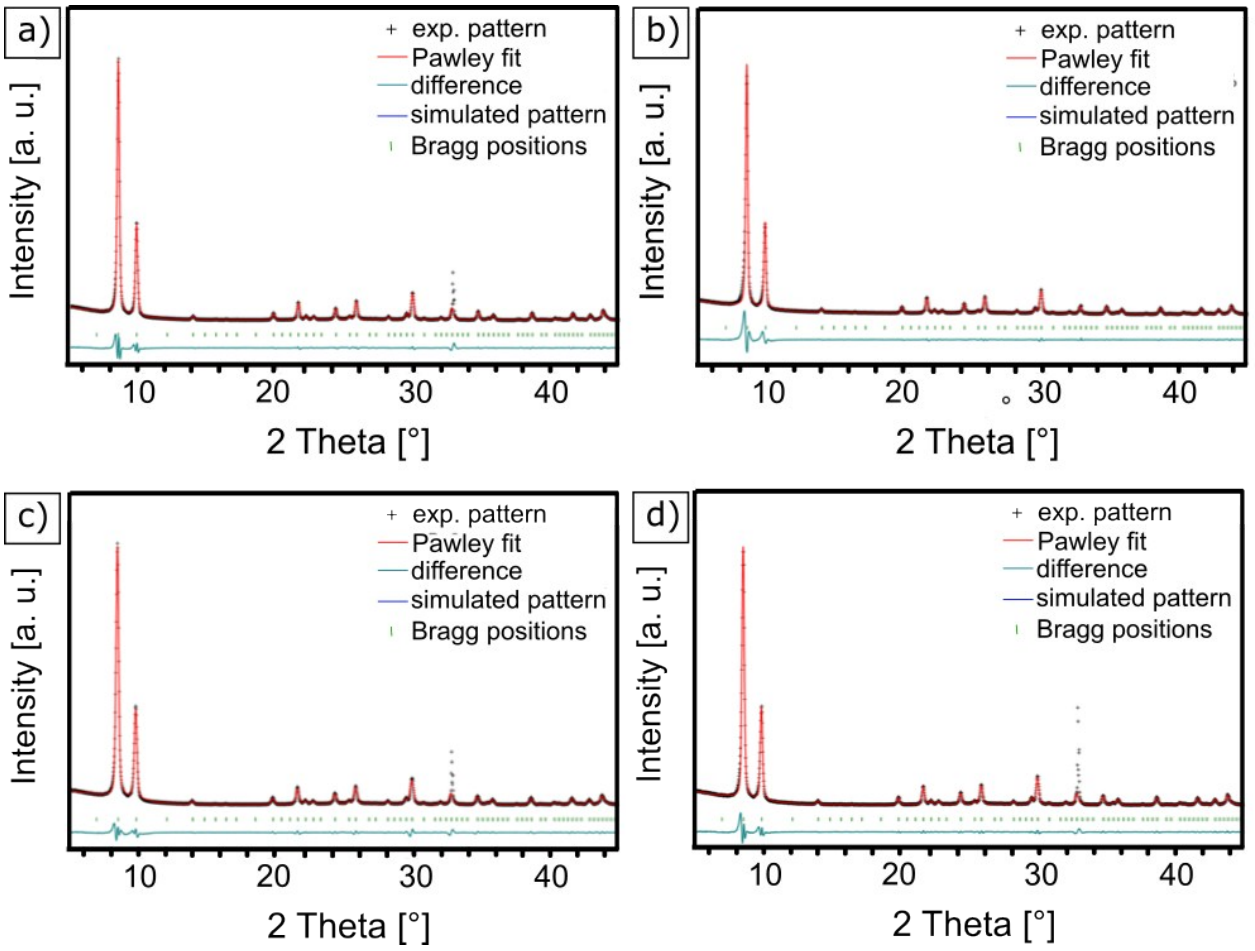

Figure S14 | PXRD patterns of the Zrfum-1 (a), Zrfum-2 (b), Zrfum-3 (c), and Zrfum-4 (d). The experimental data are shown in black, corresponding Pawley fits in red, Bragg positions as green symbols, and the difference between the experimental pattern and the fits as dark green lines. All four experimental patterns were found to feature an additional peak at 31.5 ° of variable intensity, which could not be attributed to any of the starting materials or the MOF. This reflection was masked during the Pawley fitting.

Table S3 | Results of the Pawley fitting of the Zrfum-1-4 samples

Sample	Zrfum-1	Zrfum-2	Zrfum-3	Zrfum-4
Space Group	$Pn\bar{3}$	$Pn\bar{3}$	$Pn\bar{3}$	$Pn\bar{3}$
R_p [%]	10.00	14.11	9.45	10.61
R_{wp} [%]	6.79	13.22	4.92	7.79
Lattice parameter *a* [Å]	17.91 ± 0.03	17.89 ± 0.03	17.89 ± 0.03	17.88 ± 0.03
Average domain size *d* [nm]	60 ± 5	55 ± 5	42 ± 5	54 ± 5

Atomic Force Microscopy

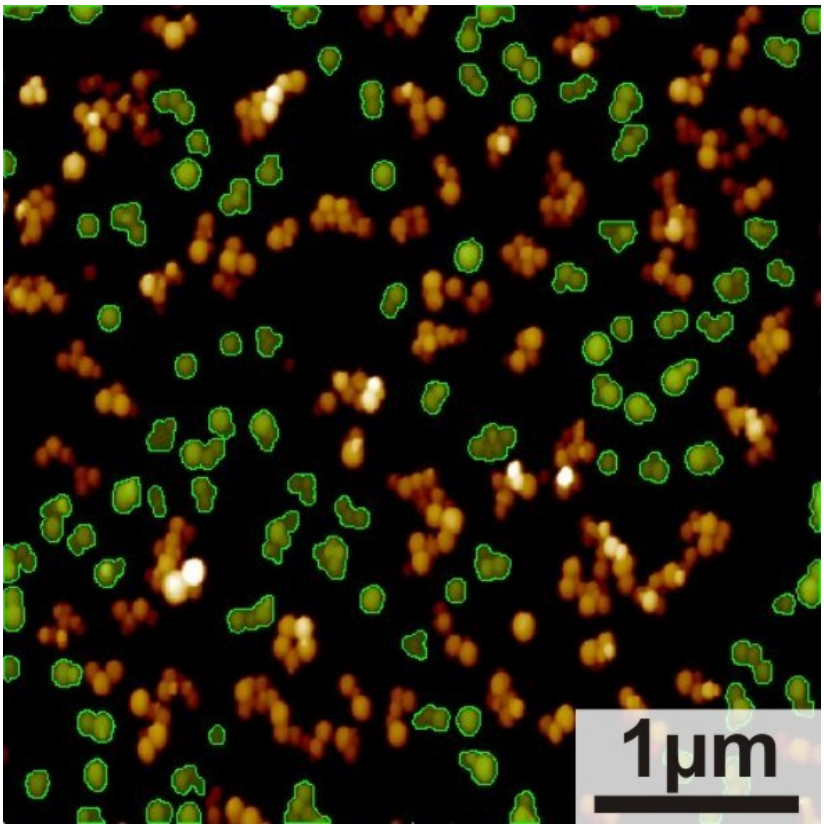

Figure S15 | AFM image of MOFs after performing particle and pore analysis in Scanning Probe Image Processing (SPIP). The maximum height of green coloured areas was determined with respect to the surrounding substrate (black). Among chosen particles agglomeration in image plane is clearly observable. However, data indicated no stacking in evaluated z-direction.

In Figure S16 a zoom-in is shown (a), together with an exemplary topographical cross-section of a single particle (b). For a quantitative particle size analysis, only the height was used, since the lateral extension is mainly given by the apex of the AFM tip and thus appears larger than the height (cf. Figure S16 b).

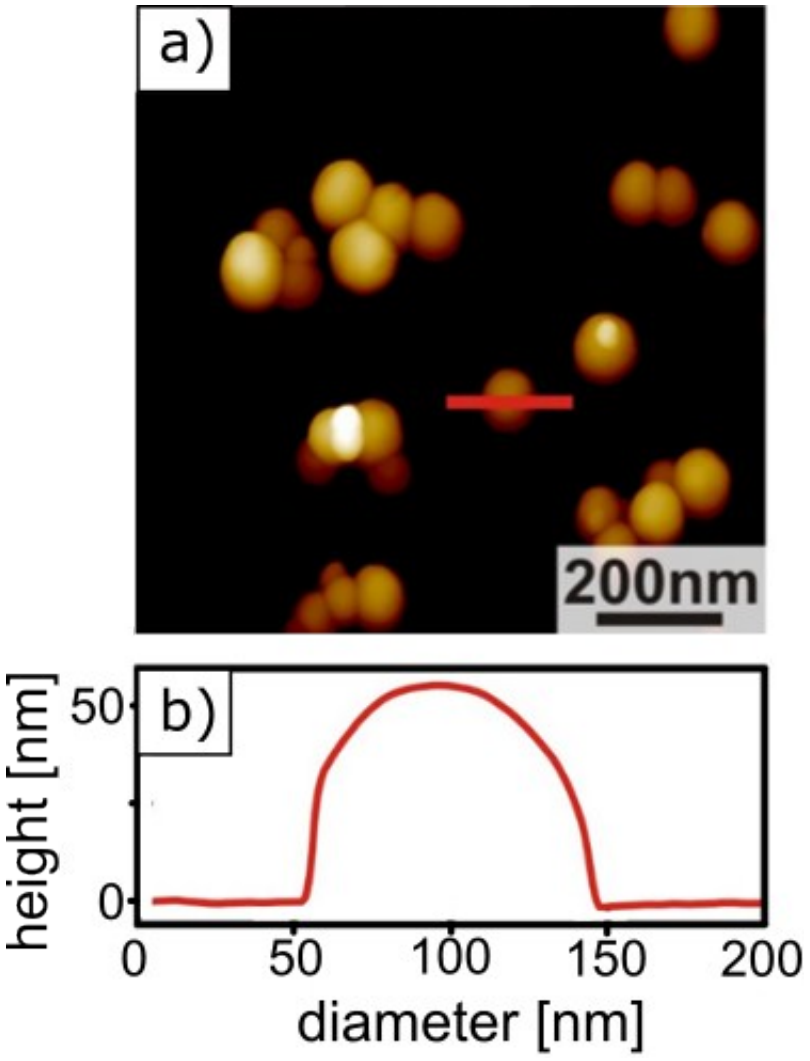

Figure S16 | Zoomed-in AFM micrograph (a) with corresponding cross section of one single particle (b).

2.4 Ensuring Reproducibility

To ensure reproducibility in the synthesis of the Zr-*fum* nanoparticles, multiple batches (Zrfum-1 to Zrfum-4) were synthesised and examined for their size attributes. This was done with X-ray diffraction, additionally with dynamic light scattering in ethanol.

Dynamic Light Scattering

The particle size distribution of samples Zrfum-1, Zrfum-2, Zrfum-3, and Zrfum-4 were determined *via* dynamic light scattering in ethanol. The results are shown in Table S4. Each sample was measured two consecutive times after finishing the washing steps of the synthesis. The similarities in the resulting diameters ranging from 129 nm to 136 nm show the good reproducibility of the synthesis of the particles. However, there are fluctuations regarding the polydispersity index (PDI), even for two consecutive measurements of the same sample, which shows, that the PDI can only be used as a rough estimation for the polydispersity of the sample.

Table S4 | Results (intensity distribution) of the DLS measurements of samples Zrfum-1 to Zrfum-4 in ethanol.

Sample	Measurement	Diameter(Cumulants) [nm]	PDI
Zrfum-1	1	130	0.135
	2	129	0.168
Zrfum-2	1	135	0.094
	2	132	0.136
Zrfum-3	1	135	0.098
	2	135	0.111
Zrfum-4	1	136	0.117
	2	134	0.086

Fluorescence Correlation Spectroscopy

The particle size and size distribution of samples Zrfum-1, Zrfum-2, Zrfum-3 were determined with FCS. The results are shown in Table S5. The similarities in the resulting diameters show the good reproducibility of the synthesis of the particles.

Table S5 | Results of the FCS measurements of samples Zrfum-1 to Zrfum-3 labeled with Alexa Fluor 488 in water. FWHM = full width at half maximum

Sample	Diameter (single component Fit) [nm]	Diameter & FWHM (GDM Fit, see calculations) [nm]
Zrfum-1	127	133, 12
Zrfum-2	136	133, 18
Zrfum-3	136	135, 17

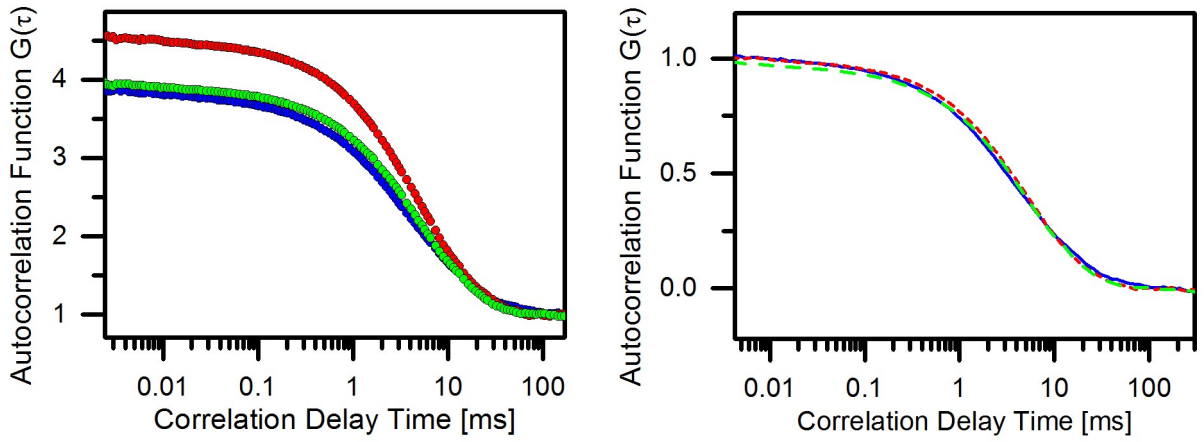

Figure S17 | FCS Autocorrelation functions of labelled Zr-fum particles sample 1(blue), 2(red) and 3(green). Original correlation curves (left) show slightly different correlation heights implying slightly different concentrations of the three nanoparticle samples. The same data after normalisation (b) shows small variation in the diffusion times of the Zr-fum samples denoting small batch to batch variations in the hydrodynamic diameter which was also confirmed by single component and GDM fit.

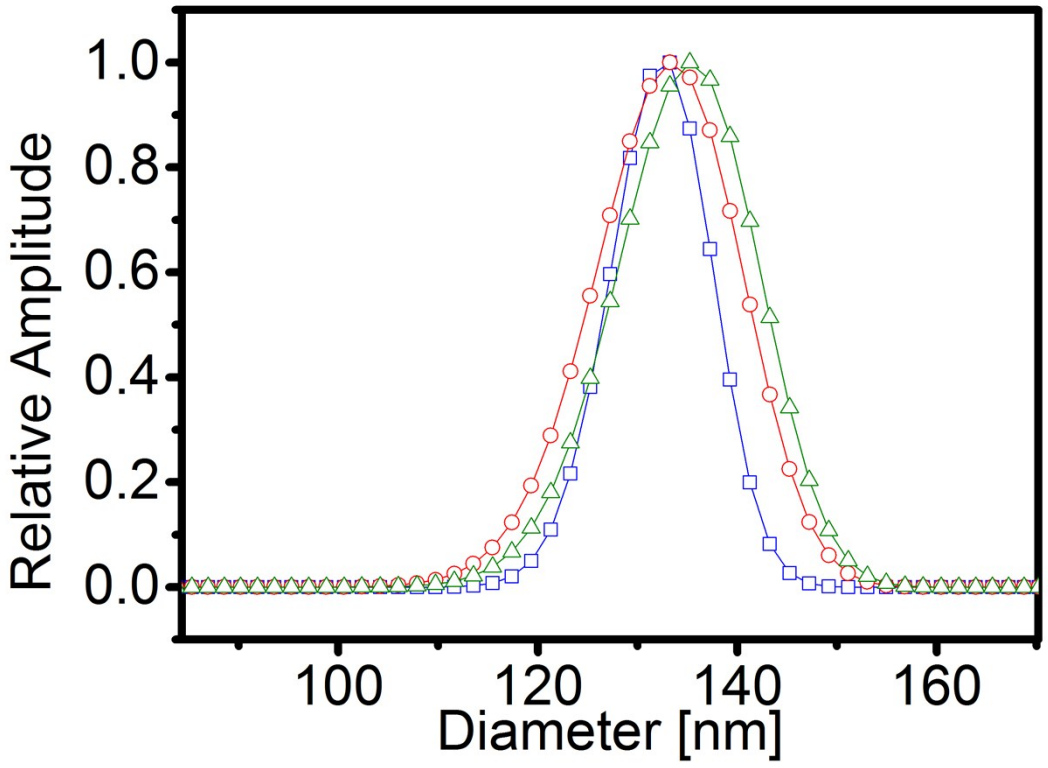

Figure S18| FCS size distribution of three measured nanoparticle batches 1(blue), 2(red) and 3(green) obtained from GDM Fit. The similarities in the resulting diameters show the great reproducibility of the synthesis of the particles.

3 Calculations

3.1 Dynamic Light Scattering

The data received during the DLS measurements was evaluated using the "method of cumulants"[7], which is shortly described in the following section. It introduces a polydispersity index (PDI, see equation (6)) as an indicator of the size distribution of the particles. Generally, DLS uses the time-dependent intensity fluctuations of a sample-scattered laser. These intensity fluctuations can be described with a second order intensity-autocorrelation function as shown in equation (1):

$$G^{(2)}(\tau) = \frac{\langle I(t)I(t\ +\ \tau)\ \rangle}{\langle I(t)\rangle^2} \tag{1}$$

The intensity-autocorrelation function is linked by the Siegert relation[8] to a field-correlation function as presented in equation (2), using the baseline *B* and a geometry factor β.

$$G^{(2)}(\tau) = B + \beta[g^{(1)}(\tau)]^2 \tag{2}$$

This field-correlation function of monodisperse particles can be described with equation (3) featuring the decay rate Γ and the passed time τ:

$$G^{(1)}(\tau) = \exp\,(-\Gamma\tau) \tag{3}$$

The decay rate $\Gamma = Dq^2$ includes the diffusion coefficient *D* and the magnitude of the scattering vector *q*, which is given by equation (4):

$$q = \frac{4\pi n}{\lambda_0} sin\left(\frac{\theta}{2}\right) \tag{4}$$

Here, *n* is the refractive index of the solvents, θ is the angle at which the scattered intensity was measured (θ = 173 °), and λ_0 is the wavelength of the laser in vacuum (λ_0 = 633 nm).

For polydisperse samples, the "method of cumulants" can be used. Here, the intensity-autocorrelation function is described by equation (5):

$$G^{(2)} = B + \beta \exp(-2\bar{\Gamma}\tau)\left(1 + \frac{\mu_2}{2!}\tau - \frac{\mu_3}{3!}\tau^2 \ldots\right)^2 \quad (5)$$

With this method, the correlation function was fitted up to the point, where the amplitudes are 10% of the initial amplitude. The term $\left(1 + \frac{\mu_2}{2!}\tau - \frac{\mu_3}{3!}\tau^2 \ldots\right)$ was cut off at its second segment. Using this method of cumulants, it is possible to take into account multiple species in dispersion. It introduces a polydispersity index (PDI, see equation (6)) as an indicator of the size distribution of the particles.

$$PDI = \frac{\mu_2}{\bar{\Gamma}^2} \quad (6)$$

This polydispersity index was used to determine the standard deviation σ of the particle size distribution using equation (7) with the average hydrodynamic particle diameter *d.*

$$PDI = \left(\frac{\sigma}{d}\right)^2 \quad (7)$$

3.2 Fluorescence Correlation Spectroscopy

Fluorescence correlation spectroscopy (FCS) is a versatile technique that makes use of fluorescence intensity fluctuations to characterise the dynamics of a low number of particles (e.g. single molecules or nanoparticles) diffusing through a very small confocal detection volume. It has been used in plentiful biophysical studies and many applications in analytical chemistry and Biochemistry were found.[9-12] FCS is ideal for measuring molecular diffusion and, thus, the molecular size in highly dilute solutions without any need to perturb the system.[13, 14]

Since Magde *et al.* demonstrated the principles of FCS in 1972 and improvements of Rigler *et al.* using confocal microscopy, FCS evolved immensely in terms of its applicability, sensitivity and versatility.[15, 16]

In FCS, information is extracted by determination of the autocorrelation function (equation (8))

$$G(\tau) = \frac{\langle F(t)F(t+\tau)\rangle}{\langle F\rangle^2} \tag{8}$$

of the fluctuating fluorescence signal F(t) and fitting an physical model to the resulting correlation curve. In the case of free diffusion the correlation is given by equation (9),

$$G(\tau) = 1 + G(0)\frac{1}{1+\frac{\tau}{\tau_D}}\frac{1}{\sqrt{1+\frac{\tau}{S^2\tau_D}}}, \tag{9}$$

where $G(0)$ is the correlation's amplitude, S is the ratio between the lateral and the axial confocal volume radius, while τ_D is the mean time a particle needs to diffuse across the focal volume[17]. Knowing the width ω of the confocal volume, the hydrodynamic radius is given by equation (10)

$$R_H = \frac{2k_B T\tau_D}{3\pi\eta\omega^2} \tag{10}$$

using the Boltzmann constant k_B as well as the temperature $T = 295\,\mathrm{K}$ and viscosity $\eta = 0.958\,\mathrm{mPas}$ of the measured aqueous suspension.

In order to obtain a size distribution from FCS fits a Gaussian Distribution Model (GDM) fit[12] was also applied. The underlying concept of GDM is that the sample is not monodisperse with a single value for the diffusion time, τ_D, but a Gaussian distribution on a fixed logarithmic diffusion time-scale with a peak diffusion time τ_P. The fit to the autocorrelation function is described by equation (11)

$$G(\tau) = 1 + \sum_{i=1}^{n} a_i(\tau_{Di})\frac{1}{1+\frac{\tau}{\tau_{Di}}}\frac{1}{\sqrt{1+\frac{\tau}{S^2\tau_{Di}}}}, \tag{11}$$

where $a_i(\tau_{Di}) = \mathrm{A}\exp\left[-\left(\frac{\ln\left(\frac{\tau_{Di}}{\tau_P}\right)}{b}\right)^2\right]$ with relative amplitude *A* and a distribution width of *b*.

Taking into account that Zr-fum nanoparticles have radii comparable to the beam waist ω, the measured diffusion time has a larger value than it would have if point particles with the same diffusive behavior were observed. Due to the fact that Alexa Fluor 488 labeling was applied at the outer surface of the nanoparticles they are fluorescing hollow spheres from the FCS view. The equation $\tau_{measured} = \tau_{D_{pointparticle}} \cdot (1 + \frac{8R^2}{3\omega^2})$, taken from Wu et al. [18] was used to correct this finite particle size effect of hollow spheres.

4 References

1. S. Brunauer, P. H. Emmet and E. Teller, *J. Am. Chem. Soc.*, 1938, **60**, 309-319.
2. G. S. Pawley, *J. Appl. Cryst.*, 1981, **14**, 357-361.
3. Z. Petrásek and P. Schwille, *Biophys J.*, 2008, **94**, 1437-1448.
4. G. Persson, P. Thyberg, T. Sandén and J. Widengren, *J. Phys. Chem. B*, 2009, **113**, 8752-8757.
5. G. Wißmann, A. Schaate, S. Lilienthal, I. Bremer, S. A. M and B. P, *Microporous Mesoporous Mater.*, 2012, 64-70.
6. K. S. W. Sing, D. H. Everett, R. A. W. Haul, L. Moscou, R. A. Pierotti, J. Rouquérol, T. Siemieniewska, *Pure & Appl. Chem.*, 1985, **57**, 603-619.
7. B. J. Frisken, *Appl. Opt.*, 2001, **40**, 4087-4091.
8. K. Schätzel, *"Single-photon correlation techniques" in Dynamic Light Scattering, W. Brown*, Oxford University, 1993.
9. M. A. Digman and E. Gratton, *Annu. Rev. Phys. Chem.,* 2011, **62**, 645-668.
10. E. Haustein and P. Schwille, *Annu. Rev. Biophys. Biomol. Struct.,* 2007, **26**, 151-169.
11. J. J. Mittag, S. Milani, D. M. Walsh, J. O. Rädler and J. J. McManus, *Biochem. Biophys. Res. Commun.*, 2014, **448**, 195-199.
12. S. Lippok, T. Obser, J. P. Müller, V. K. Stierle, M. Benoit, U. Budde, R. Schneppenheim and J. O. Rädler, *Biophys. J.*, 2013, **105**, 1208-1216.
13. C. L. Kuyper, K. L. Budzinski, R. M. Lorenz, Chiu and D. T., *J. Am. Chem. Soc.*, 2006, **128**, 730-731.
14. N. Pal, S. D. Verma, M. K. Singh and S. Sen, *Anal. Chem.*, 2011, **83**, 7736-7744.
15. D. Madge, E. Elson and W. W. Webb, *Phys. Rev. Lett.*, 1972, **29**, 705-708.
16. R. Rigler, Ü. Mets, J. Widengren and P. Kask, *Eur. Biophys. J.*, 1993, **22**, 169-175.
17. P. Schwille and E. Hausstein, *Anal. Chem.*, 2009, **94**, 1-33.
18. B. C. Wu, Yan, Müller, Joachim D., *Biophys. J.*, 2008, **7**, 2800-2808.